Supporting Information for

Direct Observations of the Rotation and Translation of Anisotropic Nanoparticles Adsorbed at a Liquid-Solid Interface

See Wee Chee,[1, 2, 3, #] Utkarsh Anand,[1, 2, 3, #] Geeta Bisht,[1, 2] Shu Fen Tan,[1, 2] and Utkur Mirsaidov[1, 2, 3, 4, 5,*]

[1] Department of Physics, National University of Singapore, Singapore 117551

[2] Centre for BioImaging Sciences, Department of Biological Sciences, National University of Singapore, Singapore 117557

[3] Centre for Advanced 2D Materials and Graphene Research Centre, National University of Singapore, Singapore 117546

[4] NUSNNI-NanoCore, Faculty of Engineering, National University of Singapore, Singapore 117581

[5] Department of Materials Science and Engineering, National University of Singapore, Singapore 117575

# Contributed equally

* Correspondence: mirsaidov@nus.edu.sg

Table of Contents

1. Calibration of electron flux and liquid thickness measurements

The electron flux is pre-calibrated prior to the start of experiments using the electron current reading reported by the TEM and with no sample in the beam path. Thereafter, we keep the beam illumination fixed to two sizes that differ by ~33 %. The electron flux is changed further by going from spot size 1 to spot size 5 at each illumination size. This change results in a drop of ~60 % in the electron flux, giving us the four combinations, 50 $e^-/(Å^2 \cdot s)$ to 20 $e^-/(Å^2 \cdot s)$, and 80 $e^-/(Å^2 \cdot s)$ to 30 $e^-/(Å^2 \cdot s)$.

The liquid layer thickness was estimated using the electron energy loss spectrum (EELS) obtained from the imaged area. The details of this procedure can be found in our previous paper and the references therein.[1] In short, the measurement is based on Beer's law and the thickness is calculated from the ratio of integral intensities between the zero-loss peak and the entire EELS spectrum.

2. Image processing and analysis

The automated nanoparticle (NP) segmentation and tracking algorithms were implemented in Python-2.7,[2] using scientific packages *numpy*,[3] *scipy*,[3] *opencv*,[4] *scikit-image*,[5] *cython*,[6] and libraries such as *matplotlib*,[7] *pims*, and *hyperspy*.[8] The NP segmentation procedure is summarized in Figure S1. First, the raw image was inverted, and then, high-frequency noise was removed using a median filter with a square of 10 pixels × 10 pixels as a structuring element. After normalizing the intensity of the filtered image, the NP contrast was enhanced. Next, we found the position of the NP using the Laplacian of Gaussian (LoG) filter with typical values for the Gaussian parameter being σ = 20 pixels and threshold = 0.15 (the LoG filter is implemented as the *blob_log* function in the *scikit-image* Python library). Finally, a region of interest (ROI) was selected around the identified NP and the intensity values were fitted to a 2-dimensional Gaussian function (Eq. S1) to get a tight fit of the NP orientation and size.

$$f(r,c) = A\exp\left[-\left(\frac{(r-\mu_r)^2}{\sigma_r^2} + \frac{(c-\mu_c)^2}{\sigma_c^2} - \frac{2\rho(r-\mu_r)(c-\mu_c)}{\sigma_r\sigma_c}\right)\left(\frac{1}{2(1-\rho^2)}\right)\right] \quad \text{(Eq. S1)}$$

Here, μ_r, μ_c, σ_r, σ_c, and ρ are Gaussian means along the rows and columns of the image, standard deviations along the rows and columns, and correlation term, respectively.

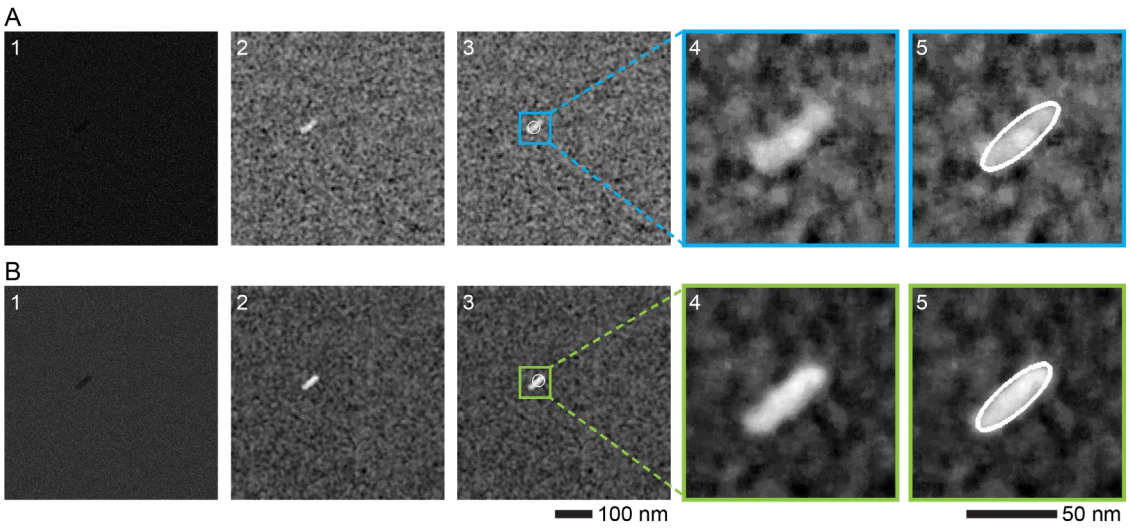

Figure S1. Step-by-step procedure for NP segmentation. (**A**) Low electron flux image (8 $e^-/(Å^2 \cdot s)$, 300 fps). Left to right: 1 – Raw image captured by TEM, where the NR is barely visible. 2 – Processed image. The raw image is subject to (*i*) intensity inversion, (*ii*) median filter, followed by (*iii*) intensity normalization between 0 (black) and 255 (white). 3 – Isolating the region of interest using the LoG method. 4 – Cropped ROI after isolating the location of the NR. 5 – The final fit boundary is overlaid on the cropped image and is represented as a white ellipse boundary. (**B**) High electron flux image (50 $e^-/(Å^2 \cdot s)$, 300 fps).

After segmenting all the frames, the identified NPs were stitched together across time. To do so, we generated a 3-dimensional binary volume stack using the segmented image sequence containing the NPs of interest where the *z*-direction represents time. Then, each NP in the volume stack was labeled across different time points based on its area and position. If the change in the NP area between the two consecutive frames was less than 10 %, and the change in the NP centroid position was less than 50 pixels, they were treated as the same object. Each *z*-slice of the labeled volume stack tracks the centroid, area, perimeter, and boundary of the NPs.

***Identification of incorrect segmentation*:** The nanorods (NR) and nanobipyramid (NBPs) were segmented using a 2-dimensional ellipse fitting method, but images with low signal-to-noise ratio (*i.e.*, low electron flux) can generate false positives during the fitting. In order to remove the false positives, we checked the results using a template matching method in the *opencv* library to identify incorrect fits. Figure S2 summarizes the template matching procedure for false positive identification. Then, the detected false positives were removed.

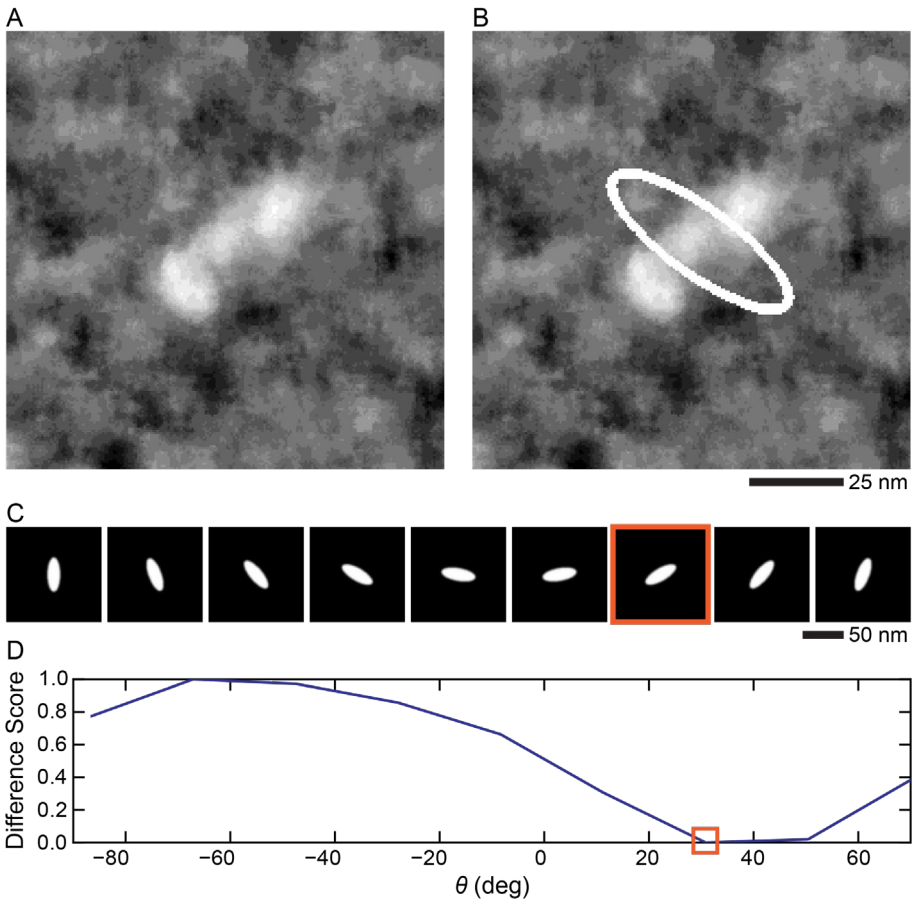

Figure S2. Template matching for identification of false positives. (**A**) ROI after identification of blobs using the LoG operator. (**B**) Best-fit result for 2-dimensional Gaussian fit on the ROI using Eq. S1. The fitting result is sensitive to an initial guess value and can converge to the incorrect ellipse (boundary drawn in white color on the image). To identify and remove the false positives, we use template matching as a secondary check on the segmentation results. (**C**) The template is a grayscale ellipse of roughly the same size as that of the NR/NBP in different orientations ranging from -90° to 80° with an interval of 20°. The templates are of the same size as that of the cropped image after locating the ROI. (**D**) The difference score of each template with the ROI is calculated using *opencv* library. The normalized difference score for each of the templates is plotted as a function of template ellipse orientation (θ). Lower difference score corresponds to a better fit of the template with ROI image. For the example illustrated above, the template ellipse oriented at 30° provides the best match (Red box; the corresponding best match template is highlighted in a red box in (C)).

3. Electron beam related effects

The probability density functions in Figure 2B for NR displacements indicate that NR2 performed several displacements (up to ~100 nm) longer than the largest displacement found for NR1 (~30 nm). Two factors can explain this seemingly different behavior between the NR1 and NR2. First, the initial illumination of NPs by the electron beam and the start time of a movie can vary by a few seconds because we waited for mechanical drift in the TEM stage to settle before recording. Therefore, there is a small uncertainty in the initial electron fluence between the two movies even though both are recorded at 50 e^-

/(Å^2·s). Second, how the dynamics evolves with time also depend on the interactions between the NP and surface. The exact time at which the NP starts to move is subject to the strength of the attractive interaction at its initial adsorption site and the random process of NP release from this site. The delay time between the initial illumination of NPs and NP motion has also been reported in other studies.[9] As highlighted in the manuscript, we attribute this lag to the time required for the radiolysis products of water to reach their steady-state concentrations.

The primary by-products are generated by the radiolysis of water are solvated electrons (e_{aq}^-), hydroxyl free radicals (OH•), hydrogen free radicals (H•), and molecular hydrogen (H_2), where the first two products are the dominant reactive species.[10] Here, we discuss the likelihood of these radicals damaging the SiN_x surface or damaging the CTAB molecules on the NP surface. We have shown in our previous paper[1] and in this current work that the NP mobility changes according to the electron flux when we increased and decreased the flux between 20 e^-/(Å^2·s) to 100 e^-/(Å^2·s) during the experiment. Therefore, it is unlikely that the electron beam permanently changed the surface groups on SiN_x. We also reiterate here the NR in Movie S5 was imaged at 20 e^-/(Å^2·s) for ~120 s (roughly the same fluence as the 80 e^-/(Å^2·s) movie) and it was largely immobile until we raised the electron flux to 50 e^-/(Å^2·s). It shows that the NR had retained its surface charge. Furthermore, degradation of the CTAB molecules should lead to the loss of positive NP surface charge and result in stronger adsorption to the surface. Hence, the CTAB molecules on the NRs also appear to be intact.

On a related note, we do not expect the electron beam to change the surface charge of the NPs significantly because it is controlled by the surface coverage of CTAB as discussed later in Supporting Section 5.

4. Estimating the displacement of a NR in bulk water

The translational diffusion coefficient, D_{rod}, of a NR in bulk water can be calculated using the following relationship:[11]

$$D_{\text{rod}} = \frac{k_B T}{3\pi\eta L}\left[\ln\left(\frac{L}{d}\right) + \upsilon\right] \quad \text{(Eq. S2)}$$

where $\eta = 8.9 \times 10^{-4}$ Pa·s is the viscosity of water, $k_B = 1.38 \times 10^{-23}$ J/K is the Boltzmann constant, and T is the temperature of the water. L and d are the length and diameter of the NR, respectively. Here, υ is given by:

$$\nu = 0.312 + 0.565\frac{d}{L} - 0.1\left(\frac{d}{L}\right)^2 \quad \text{(Eq. S3)}$$

Using equations S2 and S3, we obtain a value of $D_{rod} = 1.6 \times 10^{-11}$ m^2/s for 50 nm × 15 nm NRs. Next, the average displacement of a NR in bulk water at $T = 295$ K is calculated using:

$$\langle \boldsymbol{r}^2 \rangle = 4D_{rod}t \quad \text{(Eq. S4)}$$

where $\langle \boldsymbol{r}^2 \rangle$ is the mean square displacement of the NR. We find the average displacement for a time interval of $t = 3.3$ ms to be $\sqrt{\langle \boldsymbol{r}^2 \rangle} = 460$ nm, or ~5 times larger than the biggest jump we observe inside the liquid cell.

Here, we also estimate the likelihood that a desorbed NP will be recaptured by its original pinning site in the manner shown in Movie S7 using simple geometric considerations. We assume that a NP had desorbed and moved 100 nm to P (longest displacement we observed) from its first pinning site (denoted as O) after which the NP is free to move in any direction. Then, the probability that the NP at the second pinning point P will enter the region highlighted in blue can be calculated using the angle subtended by the region on point P (Figure S3). The size of this blue region is chosen to match a pinning site with a diameter of 50 nm. Thus, $\theta = \sin^{-1}\frac{1}{4} = 14.5^{o}$ and the probability that the NP will be captured again by the same pinning site is $\sim {}^{2\theta}/_{360^{o}} = 0.08$ or 8 %.

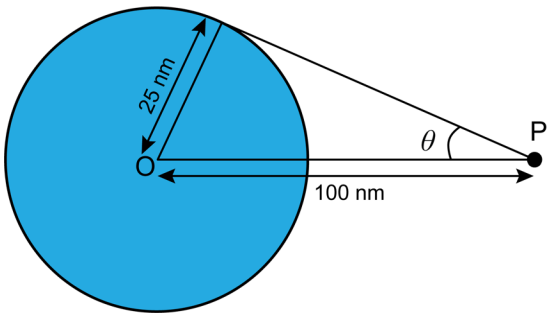

Figure S3. Probability of a NP at P to revisit the pinning site at O. The NP is free to move in any direction and the likelihood of visiting the blue region can be calculated geometrically. The blue area denotes a pinning site that is 50 nm in diameter.

5. Estimating the change in surface charge using DLVO theory

The volumes of NRs and NBPs are ~9000 nm^3 and ~40000 nm^3, respectively. ζ-potential for these NPs were measured as 6.8 mV for NR and 8.2 mV for NBP.[12] Assuming the surface potential for these NPs is 1 order of magnitude larger than the measured ζ-potential, and considering metal spheres of

equivalent volume, we calculated the net charge on the NR and NBP as +0.6e and +1.2e, respectively. We attributed the net charge on these NPs to their CTAB capping, which have an effective length of ~2 nm.[13,14]

Next, we used finite element modeling to calculate the electrostatic interaction potential. First, we constructed the entire volume of a NR (length: $L = 50$ nm, diameter: $2R = 15$ nm) and SiN_x surface ($L = 50$ nm, $W = 50$ nm, $H = 1$ nm) using spheres of 1 nm in diameter (Figure S4). For these NPs, we assumed that the surface charge would be controlled by the surface coverage of CTAB molecules on the different facets. For the NRs, it is known that CTAB molecules prefer to bind to the {100} and {110} facets that make up the NR shaft over the {111} facets that make up the NR tips.[15] Hence, the surface charge will be lower at the tip. The pentagonal NBPs, on the other hand, are predominantly made up of {111} facets. In this case, the NBP should be uniformly charged. The tips of the NBPs may have CTAB coverage different from the faces, but we still do not have details about the surface facets of the NBP tips.

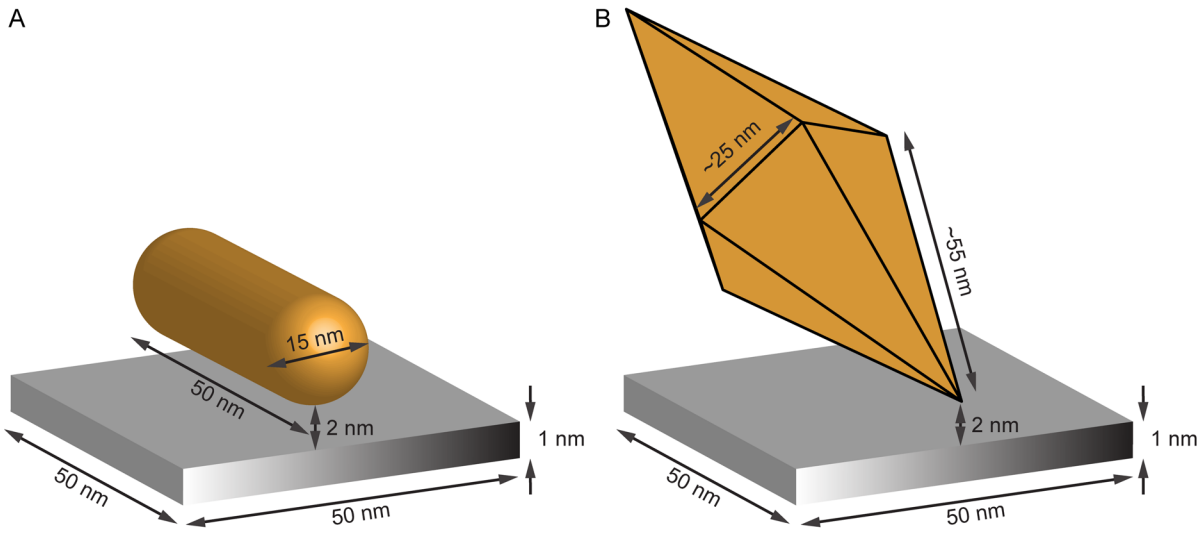

Figure S4. NR and NBP models for calculating the interaction potentials using the DLVO theory. (**A**) The NR ($L = 50$ nm, $2R = 15$ nm) was placed on top of a SiN_x surface ($L = 50$ nm, $W = 50$ nm, $H = 1$ nm). The NR and SiN_x were constructed with 1 nm spheres. The distance between the NR and SiN_x was fixed at 2 nm. The NR tips have a lower charge density than the shaft. (**B**) The pentagonal NBP ($L = 100$ nm, side lengths of ~25 nm and ~55 nm) was placed on top of a SiN_x surface ($L = 50$ nm, $W = 50$ nm, $H = 1$ nm) such that one triangular face of the NBP is parallel to the surface and separated by 2 nm.

The NR is constructed such that it has a cylindrical shaft ($L = 35$ nm, $R = 7.5$ nm) and spherical tips ($R = 7.5$ nm). We construct the NR using two objects so that the shaft and tips can be assigned a different charge density during the electrostatic interaction calculations. The SiN_x membrane was constructed using 2500 spheres, each having the same charge. Then, the electrostatic interaction potential between the sphere i of the NR and the sphere j of the SiN_x surface was calculated using:[16]

$$E = \sum_{i,j} E_{ij} = \sum_{i,j} \frac{z_i z_j e^2}{4\pi\epsilon_0 \epsilon r_{ij}} \frac{e^{-\kappa(r_{ij}-\sigma)}}{1+\kappa\sigma} \quad \text{(Eq. S5)}$$

$$\frac{1}{\kappa} = \frac{0.304}{\sqrt{[H_2O]}} \text{ (nm)} \quad \text{(Eq. S6)}$$

Here, e, ϵ_0, ϵ, r_{ij}, σ, and $1/\kappa$ are the charge of an electron, permittivity in vacuum, relative permittivity in water, center-to-center distance between the spheres i of the NR and the spheres j of the SiN_x surface, the diameter of the spheres (1 nm), and the Debye length, respectively. To calculate the Debye length, the electrolyte concentration of water was assumed to be 10^{-7} M. The sum of electrostatic interactions between all the spheres of the NR and SiN_x surface gives us the total electrostatic interaction potential. The spheres on the shaft are assigned a weight 1.0, and those at the tips are assigned a weight 0.9,[17] which means that a sphere on the shaft of the NR will have a stronger electrostatic interaction with the SiN_x surface compared to the sphere on NR tips. The constructed NR has 1928 spheres on the NR surface, and the total charge of the NR was taken as $+1e$. However, the 528 spheres on the NR tips have a charge density 0.9 times smaller than the 1400 spheres on the NR shaft. Using this information, we find $z_i \approx \frac{1}{1875}$, for all the spheres of the NR.

Next, we assume that the SiN_x membrane does not charge significantly at low electron flux (~20 $e^-/(Å^2 \cdot s)$) and so, the motion is representative of dynamics without electron beam irradiation. Then, the effective value of $z_j = \frac{31.50}{2500}$ gives an increase in the electrostatic interaction potential energy of 1 $k_B T$. In other words, there is an excess surface charge of $+1e$ per 79 nm^2 on the SiN_x membrane when the NR is imaged at 50 $e^-/(Å^2 \cdot s)$ and 80 $e^-/(Å^2 \cdot s)$, which corresponds to a surface potential of ~37 mV.

For the NBP, we performed a similar calculation with $z_i = \frac{1}{5023}$, $z_j = \frac{44.07}{2500}$, and found that there is an excess surface charge of $+1e$ per 57 nm^2 on the SiN_x membrane, which corresponds to a surface potential of ~52 mV at an electron flux of 50 $e^-/(Å^2 \cdot s)$. The difference in the calculated surface potential may be due to the difference in the surface charge distribution between the NR and NBP.

We also calculate the surface potential for a more realistic case of water with ions in solution where the ionic concentration is assumed to be 10^{-5} M. Here, there is an excess surface charge of $+1e$ per ~65 nm^2 on the SiN_x for the interaction between the NR and SiN_x, which corresponds to a surface potential of ~40 mV. Similarly, for the interaction of the NBP and SiN_x, there is an excess surface charge of $+1e$ per ~43 nm^2, which corresponds to a surface potential of ~61 mV.

6. Surface charge required to overcome attractive van der Waals interaction

We can use the finite element method described in the previous section (Supporting Section 5) to calculate the van der Waals (vdW) interaction between a NP and SiN_x surface. The vdW attractive interaction potential between a sphere i of the NP and sphere j of the SiN_x surface is calculated using:[16]

$$U_{\mathrm{vdW}} = \sum_{i,j} W_{ij} = -\sum_{i,j} \frac{A}{6}\left\{\frac{2r_i r_j}{(2r_i+2r_j+D)D} + \frac{2r_i r_j}{(2r_i+D)(2r_j+D)} + \ln\frac{(2r_i+2r_j+D)D}{(2r_i+D)(2r_j+D)}\right\} \qquad \text{(Eq. S7)}$$

Here, $A = 10 \times 10^{-20}$ J is the Hamaker constant for the interaction between Au and SiN_x interacting across water.[16] r_i, r_j, and D are the position of the sphere i in the NP, the position of the sphere j in the SiN_x, and the separation between the spheres i and j, respectively. We found that the vdW interaction of NR and NBP with the SiN_x sheet to be 9.9 $k_B T$ and 9.1 $k_B T$, respectively, when the separation between the NP and SiN_x surface is 2 nm.

Using similar calculations discussed in Supporting Section 5, we found that if the ionic concentration is 10^{-7} M, the surface potential would need to be 372 mV and 477 mV for the NR and NBP, respectively, to overcome the vdW attraction. If the ionic concentration is 10^{-5} M, the surface potential would need to be 395 mV and 533 mV for the NR and NBP, respectively.

7. Effect of surface treatments

Here, we describe the details of the different surface treatments discussed in the manuscript. The O_2 plasma treatment was performed using the SPI Plasma Prep III at 100 W for 30 min. The chamber pressure was maintained at ~650 mTorr during the treatment. The O_2 plasma treatment is also needed for good adhesion of 3-aminopropyltriethoxysilane (APTES) to the SiN_x surface. For silanization, we opted to use vapor deposition over the liquid-based protocol described in the main text ref. 47 to reduce the likelihood of inhomogeneous deposition. The silanization treatment was performed by placing the O_2 plasma treated liquid cell chips in a vacuum desiccator containing an aluminum dish with 10 µL of APTES and pumping on it with a mechanical pump for 5 min. Successful silanization was confirmed by measuring the contact angle of a water droplet on a dummy wafer before and after the treatment.

The TEM experiments were performed at 20 $e^-/(Å^2 \cdot s)$, our threshold electron flux for beam-induced NP motion for glow discharge treated liquid cells. The liquid cells were assembled using both top and bottom chips that had been treated. We also mention here that the efficacy of all three surface

treatments, glow discharge, O_2 plasma, and APTES silanization, decreases after a few hours in our laboratory environment. In the experiments comparing O_2 plasma and silanization treatments, the liquid cell assembly and TEM imaging were performed within one hour of treatment, on the same day, using the same batch of NPs and the same batch of liquid cell chips to minimize the possibility of artefacts due to sample variation.

8. Localization accuracy as a function of electron flux on the camera

In these experiments, the accuracy of pinpointing the position and orientation of the NPs in the images (*i.e.*, the localization accuracy) depends on the electron flux. The reason is that the quality of NP segmentation improves as the signal-to-noise ratio in each frame increases. Here, we measured the change in localization error as a function of electron flux (Figure S5) by imaging NRs that were dispersed and dried on a single 30 nm thick SiN_x membrane. The imaging electron flux was varied between 8 $e^-/(Å^2 \cdot s)$ to 80 $e^-/(Å^2 \cdot s)$, and the frame rates used for imaging were between 50 to 300 fps (note that we have one data point for 50 fps and four data points for 100 fps because the detector saturates when the nominal counts exceeds 100 per pixel per frame). As seen from the results, we have a larger localization error for all electron fluxes at 300 fps, with the error increasing with decreasing flux. It means that more than 80 $e^-/(Å^2 \cdot s)$ is needed to achieve optimal imaging conditions at 300 fps.

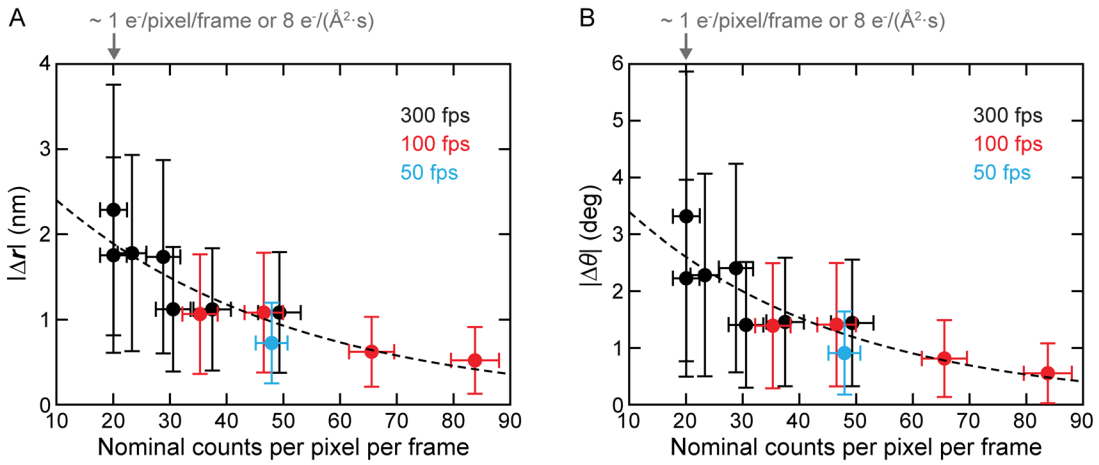

Figure S5. The change in localization error in (**A**) the position ($|\Delta \boldsymbol{r}|$) and (**B**) orientation ($|\Delta\theta|$) of a dry NR as a function of nominal counts per pixel per frame. The nominal counts are adjusted using either the acquisition rate or the incident electron flux.

We mention here that the accuracy of tracking results also depends on the inherent contrast of the imaged object. The larger pentagonal NBP (~100 nm × 40 nm) show up in the images with better contrast than the smaller NR (~50 nm × 15 nm) and is easier to track.

9. Supporting figures

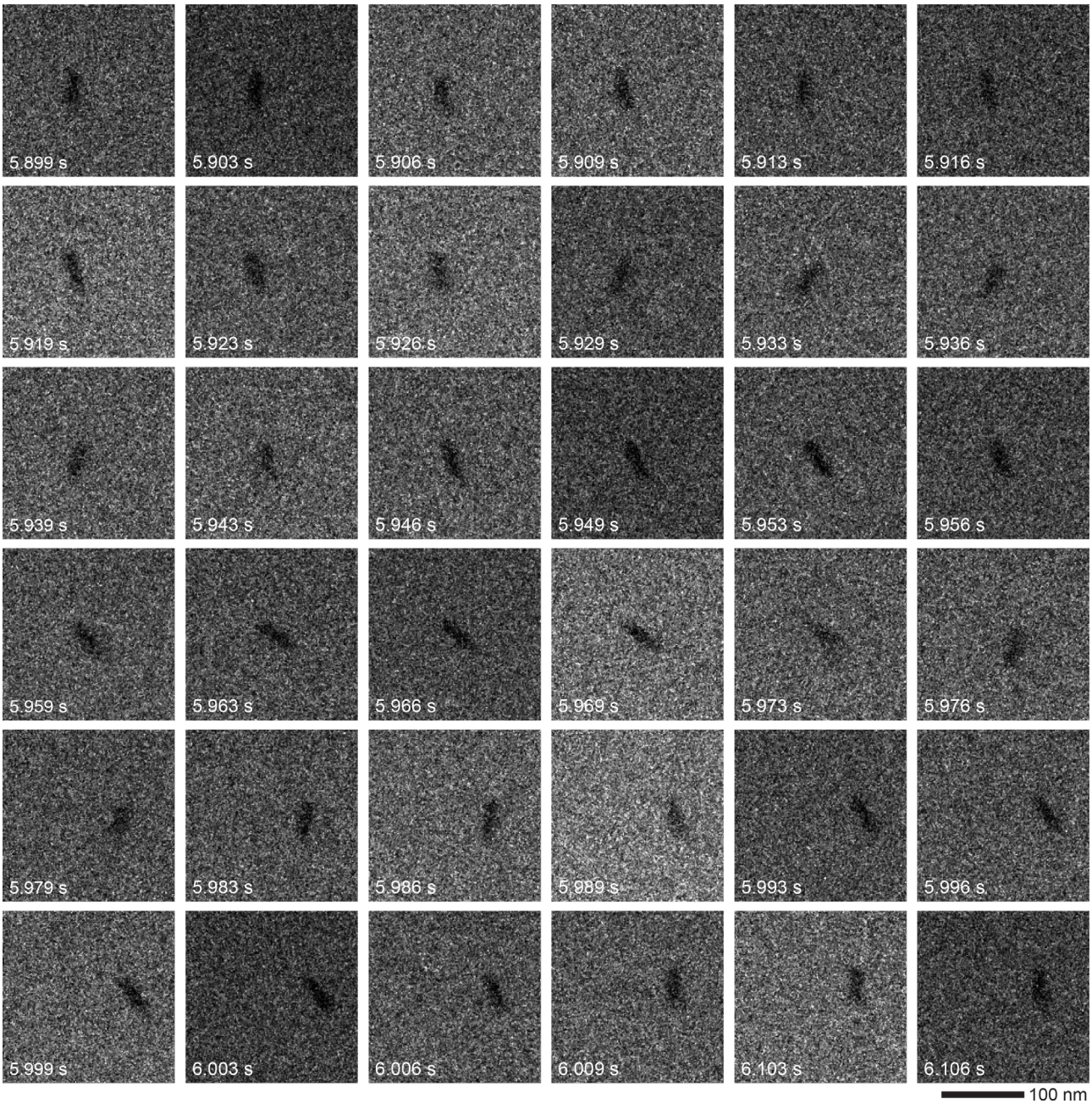

Figure S6. Image sequence for the NR presented in Figure 1C prior to the image averaging. The image sequences are acquired at an electron flux of ~50 $e^-/(Å^2 \cdot s)$.

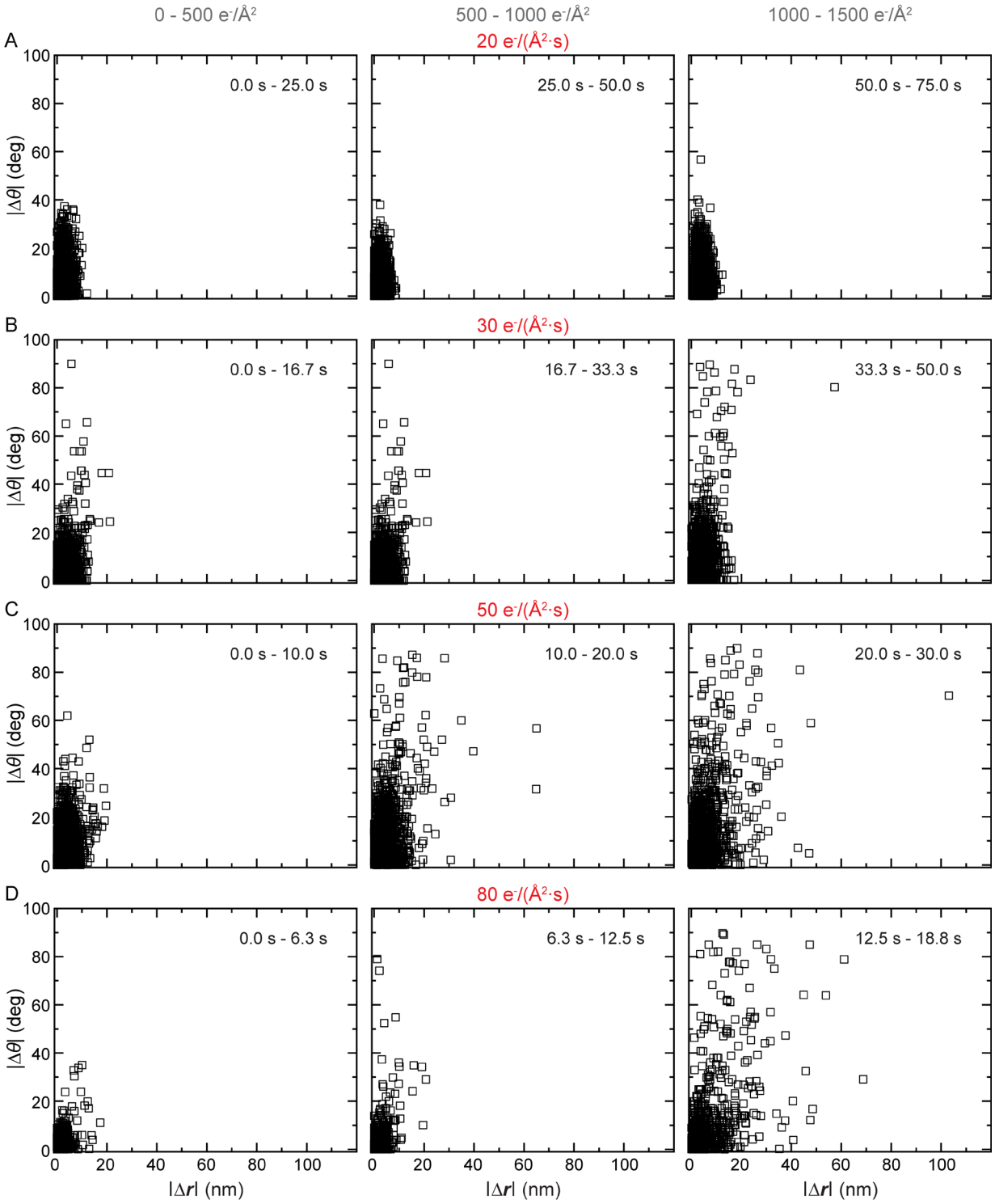

Figure S7. (**A – D**) Scatter plots describing the rotation angles ($|\Delta\theta|$) and displacements ($|\Delta\boldsymbol{r}|$) measured from each frame of the movies recorded at electron fluxes ranging from 20 – 80 $e^-/(Å^2 \cdot s)$. Each data set is normalized to have the same range of electron fluence. Hence, the panels in (A – D) have different time ranges and number of frames per plot (3.3 ms per frame). The plots illustrate three points: (1) The frequency of large displacements and rotation angles increases with the increasing electron fluence, (2) with the exception of the 20 $e^-/(Å^2 \cdot s)$ dataset, where it remains largely constant with fluence. (3) The large rotations also appear in the scatter plots before the large displacements appear, suggesting that the large rotations precede the desorption-mediated jumps.

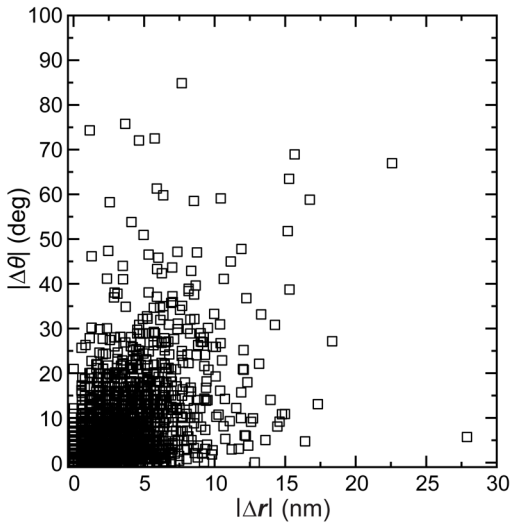

Figure S8. Scatter plot describing the rotation angles ($|\Delta\theta|$) and displacements ($|\Delta \boldsymbol{r}|$) measured from each frame of the movie for NR1 (Figure 1C and Movie S2) recorded at 50 $e^-/(Å^2 \cdot s)$. The movie duration is 11.35 s.

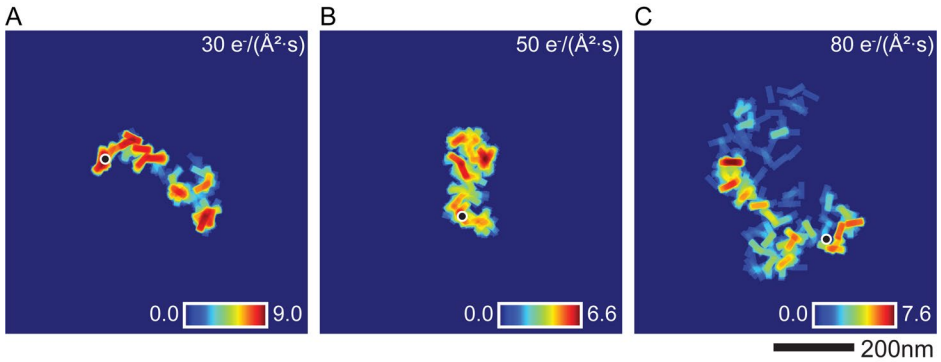

Figure S9. Residence-time maps of additional three NRs. All the NR are captured at 300 fps and imaged at (**A**) 30 $e^-/(Å^2 \cdot s)$ for 132 s, (**B**) 50 $e^-/(Å^2 \cdot s)$ for 11 s, and (**C**) 80 $e^-/(Å^2 \cdot s)$ for 23 s. The residence-time (color scale) is represented in natural logarithmic scale for clarity.

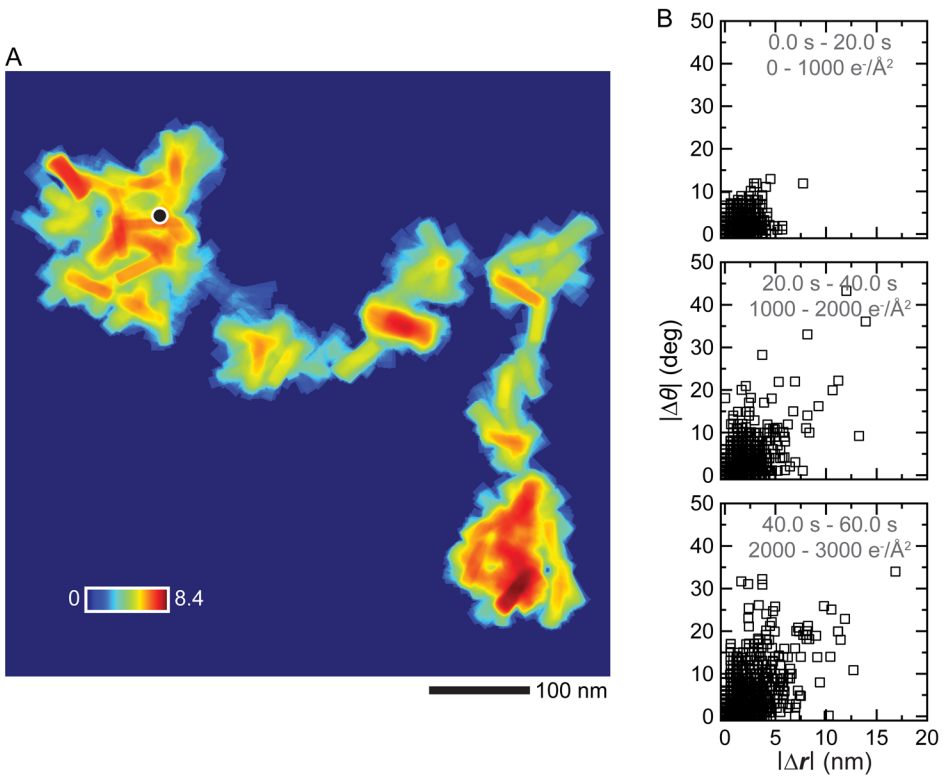

Figure S10. (**A**) Residence-time map of the positions of the NBP recorded at 50 $e^-/(Å^2 \cdot s)$ (Figure 1B and Movie S1). The residence-time (color scale) is represented in natural logarithmic scale for clarity. Initial position of the NBP is indicated with a black dot. (**B**) Scatter plot describing the displacements ($|\Delta \boldsymbol{r}|$) and rotation angles ($|\Delta\theta|$) measured from each frame of the NBP movie recorded at 50 $e^-/(Å^2 \cdot s)$. From the plots, we can see that while the rotation angles increase with fluence, the displacements remain much less than a single body length of the NBP (~100 nm). This behavior is similar to the 20 $e^-/(Å^2 \cdot s)$ dataset shown in Figure S7 where the electron flux is not enough to induce the desorption.

10. Supporting movie captions

Movie S1: Motion of a 100 nm long NBP imaged at 50 $e^-/(Å^2 \cdot s)$. The raw frames were captured at 300 fps. The image sequence was averaged by 6 to reduce the initial size of the movie. The trajectory (white line) of the NBP was overlaid on the images using Python library *matplotlib*. Then, the images are scaled down and compressed using *jpeg* compression to reduce the file size. Movie playback is in real time.

Movie S2: Motion of a 50 nm NR imaged at 50 $e^-/(Å^2 \cdot s)$. The raw frames were captured at 300 fps. The image sequence was averaged by 3. The trajectory (white line) of the NBP was overlaid on the images using Python library *matplotlib*. Then, the images are scaled down and compressed using *jpeg* compression to reduce the file size. Movie playback is in real time.

Movie S3: Motion of a second 50 nm NR imaged at 50 $e^-/(Å^2 \cdot s)$. The raw frames were captured at 300 fps. The image sequence was averaged by 3. The trajectory (white line) of the NBP was overlaid on the images using Python library *matplotlib*. Then, the images are scaled down and compressed using *jpeg* compression to reduce the file size. Movie playback is in real time.

Movie S4: Motion of four NRs imaged at 30 $e^-/(Å^2 \cdot s)$. The raw frames were captured at 300 fps. The image sequence was averaged by 3. The images are scaled down and compressed using *jpeg* compression to reduce the file size. Movie playback is in real time.

Movie S5: 20 s segment of the 50 nm NR imaged at 20 $e^-/(Å^2 \cdot s)$ where the electron flux was increased to 50 $e^-/(Å^2 \cdot s)$ at t = 10 s. The NR was imaged at 20 $e^-/(Å^2 \cdot s)$ for 120 s prior to increasing the electron flux. The raw frames were captured at 300 fps. The image sequence was averaged by 3. The images are scaled down and compressed using *jpeg* compression to reduce the file size. Movie playback is in real time.

Movie S6: Motion of a 50 nm NR imaged at 80 $e^-/(Å^2 \cdot s)$. The raw frames were captured at 300 fps. The image sequence was averaged by 3. The trajectory (white line) of the NBP was overlaid on the images using Python library *matplotlib*. Then, the images are scaled down and compressed using *jpeg* compression to reduce the file size. Movie playback is in real time.

Movie S7: Extracted sequence from Movie S6 (imaged with 80 $e^-/(Å^2 \cdot s)$ where the NR repeatedly readsorbed at the same location over a time period of 5.00 s (t = 25.00s to 31.00s). The raw frames were captured at 300 fps. The white circle with a counter denotes the area at which the NR repeatedly readsorbs. The image sequence was averaged by 3 frames. Then, the images are scaled down and compressed using *jpeg* compression to reduce the file size. Movie playback is slowed down by 5.

Movie S8: Motion of a longer 70 nm NR imaged at 50 $e^-/(Å^2 \cdot s)$. The raw frames were captured at 300 fps. The image sequence was averaged by 6. The images are scaled down and compressed using *jpeg* compression to reduce the file size. Movie playback is in real time.

11. Supporting references

(1) Chee, S. W.; Baraissov, Z.; Loh, D.; Matsudaira, P. T.; Mirsaidov, U. Desorption-Mediated Motion of Nanoparticles at the Liquid-Solid Interface. *J. Phys. Chem. C* **2016**, *120*, 20462–20470.

(2) Oliphant, T. E. Python for Scientific Computing. *Comput. Sci. Eng.* **2007**, *9*, 10–20.

(3) Van Der Walt, S.; Colbert, S. C.; Varoquaux, G. The NumPy Array: A Structure for Efficient Numerical Computation. *Comput. Sci. Eng.* **2011**, *13*, 22–30.

(4) Bradski, G. The OpenCV Library. *Dr Dobbs J. Softw. Tools* **2000**, *25*, 120–125.

(5) van der Walt, S.; Schönberger, J. L.; Nunez-Iglesias, J.; Boulogne, F.; Warner, J. D.; Yager, N.; Gouillart, E.; Yu, T. Scikit-Image: Image Processing in Python. *PeerJ* **2014**, *2*, e453.

(6) Behnel, S.; Bradshaw, R.; Citro, C.; Dalcin, L.; Seljebotn, D. S.; Smith, K. Cython: The Best of Both Worlds. *Comput. Sci. Eng.* **2011**, *13*, 31–39.

(7) Hunter, J. D. Matplotlib: A 2D Graphics Environment. *Comput. Sci. Eng.* **2007**, *9*, 99–104.

(8) Peña, F. de la; Ostasevicius, T.; Fauske, V. T.; Burdet, P.; Jokubauskas, P.; Nord, M.; Prestat, E.; Sarahan, M.; MacArthur, K. E.; Johnstone, D. N.; *et al.* Hyperspy/Hyperspy: HyperSpy 1.3, 2017.

(9) Abellan, P.; Woehl, T. J. Liquid Cell Electron Microscopy for the Study of Growth Dynamics of Nanomaterials and Structure of Soft Matter. In *In-situ Characterization Techniques for Nanomaterials*; Kumar, C. S. S. R., Ed.; Springer: Berlin, Heidelberg, 2018; pp. 1–31.

(10) Schneider, N. M.; Norton, M. M.; Mendel, B. J.; Grogan, J. M.; Ross, F. M.; Bau, H. H. Electron–Water Interactions and Implications for Liquid Cell Electron Microscopy. *J. Phys. Chem. C* **2014**, *118*, 22373–22382.

(11) Tirado, M. M.; Martínez, C. L.; de la Torre, J. G. Comparison of Theories for the Translational and Rotational Diffusion Coefficients of Rod-like Macromolecules. Application to Short DNA Fragments. *J. Chem. Phys.* **1984**, *81*, 2047–2052.

(12) Tan, S. F.; Raj, S.; Bisht, G.; Annadata, H. V.; Nijhuis, C. A.; Král, P.; Mirsaidov, U. Nanoparticle Interactions Guided by Shape-Dependent Hydrophobic Forces. *Adv. Mater.* **2018**, *30*, 1707077.

(13) Weidemaier, K.; Tavernier, H. L.; Fayer, M. D. Photoinduced Electron Transfer on the Surfaces of Micelles. *J. Phys. Chem. B* **1997**, *101*, 9352–9361.

(14) Sau, T. K.; Murphy, C. J. Self-Assembly Patterns Formed upon Solvent Evaporation of Aqueous Cetyltrimethylammonium Bromide-Coated Gold Nanoparticles of Various Shapes. *Langmuir* **2005**, *21*, 2923–2929.

(15) Murphy, C. J.; Thompson, L. B.; Chernak, D. J.; Yang, J. A.; Sivapalan, S. T.; Boulos, S. P.; Huang, J.; Alkilany, A. M.; Sisco, P. N. Gold Nanorod Crystal Growth: From Seed-Mediated Synthesis to Nanoscale Sculpting. *Current Opinion in Colloid and Interface Science*, 2011, *16*, 128–134.

(16) Israelachvili, J. N. *Intermolecular and Surface Forces: Revised Third Edition.*; Academic Press, 2011.

(17) Meena, S. K.; Sulpizi, M. Understanding the Microscopic Origin of Gold Nanoparticle Anisotropic Growth from Molecular Dynamics Simulations. *Langmuir* **2013**, *29*, 14954–14961.